

Article

New Concept for the Facile Fabrication of Core–Shell CuO@CuFe₂O₄ Photocathodes for PEC Application

Linh Trinh ^{1,*} , Krzysztof Bienkowski ¹ , Piotr Wróbel ² , Marcin Pisarek ³ , Aleksandra Parzuch ¹ , Nabila Nawaz ¹  and Renata Solarska ^{1,*} 

¹ Laboratory of Molecular Research for Solar Energy Innovations, Centre of New Technologies, University of Warsaw, 02-097 Warsaw, Poland; k.bienkowski@cent.uw.edu.pl (K.B.); a.parzuch@student.uw.edu.pl (A.P.); n.nawaz@cent.uw.edu.pl (N.N.)

² Faculty of Physics, University of Warsaw, 02-093 Warsaw, Poland; piotr.wrobel@fuw.edu.pl

³ Institute of Physical Chemistry, Polish Academy of Sciences, 01-224 Warsaw, Poland; mpisarek@ichf.edu.pl

* Correspondence: l.trinh@cent.uw.edu.pl (L.T.); r.solarska@cent.uw.edu.pl (R.S.)

Abstract: The CuO@CuFe₂O₄ core–shell structure represents a new family of photocatalysts that can be used as photoelectrodes that are able to produce hydrogen under a broad spectrum of visible light. Herein, we report a novel approach for the production of this active film by the thermal conversion of CuFe Prussian Blue Analogues. The outstanding photoelectrochemical properties of the photocathodes of CuO@CuFe₂O₄ were studied with the use of combinatory photo-electrochemical instrumental techniques which proved that the electrodes were stable over the whole water photolysis run under relatively positive potentials. Their outstanding performance was explained by the coupling of two charge transfer mechanisms occurring in core–shell architectures.

Keywords: metal oxides; spinel metal oxides; Prussian blue analogues; photoelectrochemistry; electrodeposition



Citation: Trinh, L.; Bienkowski, K.; Wróbel, P.; Pisarek, M.; Parzuch, A.; Nawaz, N.; Solarska, R. New Concept for the Facile Fabrication of Core–Shell CuO@CuFe₂O₄ Photocathodes for PEC Application. *Materials* **2022**, *15*, 1029. <https://doi.org/10.3390/ma15031029>

Academic Editor: Alberto Vertova

Received: 30 December 2021

Accepted: 25 January 2022

Published: 28 January 2022

Publisher's Note: MDPI stays neutral with regard to jurisdictional claims in published maps and institutional affiliations.



Copyright: © 2022 by the authors. Licensee MDPI, Basel, Switzerland. This article is an open access article distributed under the terms and conditions of the Creative Commons Attribution (CC BY) license (<https://creativecommons.org/licenses/by/4.0/>).

1. Introduction

Due to an increasing demand for and the limitation of fossil fuels, hydrogen fuel produced by photoelectrochemical (PEC) water splitting has been considered as a promising alternative since it is known for being clean, abundant and sustainable [1–3]. Copper ferrite (CuFe₂O₄) has been studied for its catalytic H₂ production owing to its narrow bandgap of 1.3–2 eV with a conduction band edge above 0 V vs. RHE [4]. Despite this, CuFe₂O₄ has mostly been studied as photoanodes [5–9]. There are some studies of CuFe₂O₄ as photocathodes for H₂ production and CO₂ reduction, however, most studies on these materials still have a number of challenges as CuFe₂O₄ suffers from severe photocorrosion and/or low photocurrent densities [10–14]. It has been reported that the combination of p-type Cu and α -Fe₂O₃ would be favorable for water splitting due to the shift in the conduction band edge potential, leading to a greater absorption of photons in the visible spectrum [15,16]. Recently, Park et al. [17] reported the rapid flame-annealed CuFe₂O₄ with an exceptional photocurrent density of -1.82 mA/cm² at 0.4 V RHE despite its short-term stability and heavy photocorrosion. Maitra et al. [18] proposed a wet chemistry synthetic route for a highly porous CuFe₂O₄ nanoflake where the degrees of spinel inversion (δ) of the materials were taken into account and CuFe₂O₄ prepared at medium temperature (230 °C) showed the highest photocurrent density at 0 V vs. RHE with $J = -0.99$ mA/cm²; however, its stability was not reported.

In the frame of this work, we propose a new spinel CuFe₂O₄ prepared by thermal conversion from CuFe Prussian Blue Analogues (PBAs) (formula: Cu^{II}[Fe^{III}(CN)₆]_x·xH₂O). PBAs are the derivative forms of Prussian Blue (PB) with the general formula K₄[Fe^{III}Fe^{II}(CN)₆] prepared by replacing one of the Fe ions by another transition metal [19]. These materials have a historical figure owing to their unique electronic and optical properties. The thermal

conversion of PBAs into spinel metal oxides was first proposed by Zakaria et al. [20] on FeCo PBAs, CoCo PBAs, and PB by annealing them at high temperature to eliminate the C≡N bonds between the two metal centers to form spinel CoFe_2O_4 , Co_3O_4 , and Fe_2O_3 , respectively. This conversion method has the advantage of retaining the original structure of PBAs as they possess an abundance of metal ions and high porosity. The incorporation of porous structure and noble metals into semiconductors offer a promising strategy for fabricating a structure with greater light activity due to a larger surface area which serves as a support to bind particles [21,22].

In this study, CuFe PBAs thin film was deposited on FTO glass using electrosynthesis and then annealed at 550 °C to form a CuFe_2O_4 photocathode. The photocathode had a sufficiently high photocurrent density of -0.3 mA/cm^2 with a small photocorrosion observed. Moreover, the materials were shown to have great stability over time. The materials were investigated by various techniques.

2. Materials and Methods

2.1. Preparation of $\text{CuO@CuFe}_2\text{O}_4$

The layer of $\text{CuO@CuFe}_2\text{O}_4$ on FTO glass (dimension 15 mm × 35 mm) was prepared by electrodeposition performed on Biologic SP-300 potentiostat using a conventional three-electrode system with an Ag/AgCl reference electrode, Pt wire as the counter electrode and clean FTO glass as the working electrode. First, the working electrode was applied in a constant potential of -0.9 V (vs. Ag/AgCl) for 4 min in an aqueous solution of 80 mL containing 10 mM CuSO_4 ($\text{CuSO}_4 \cdot 5\text{H}_2\text{O}$ Sigma-Aldrich 99.99% CAS: 7758-99-8), 100 mM K_2SO_4 (K_2SO_4 Sigma-Aldrich ≥ 99.0% CAS: 77778-80-5), and 1 mM H_2SO_4 for the deposition of Cu. After that, the Cu was cleaned with water and was applied at a constant potential of 0.5 V (vs. Ag/AgCl) for 30 min in an aqueous solution of 80 mL containing 10 mM $\text{K}_4[\text{Fe}(\text{CN})_6] \cdot 3\text{H}_2\text{O}$ (Sigma-Aldrich 98.5% CAS: 13746-66-2), 50 mM KCl (Sigma-Aldrich 99.0% CAS: 7447-40-7), 50 mM K_2SO_4 , and 1 mM H_2SO_4 for the formation of $\text{Cu}[\text{Fe}(\text{CN})_6]$. After a few minutes, the layer changed color from red to yellow, which is typical of $\text{Cu}[\text{Fe}^{\text{III}}(\text{CN})_6]$. After the electrosynthesis, the FTO glass was cleaned thoroughly with water and acetone and put into a furnace and annealed for one hour at 400 °C to form $\text{CuO@CuFe}_2\text{O}_4$. Then, the electrode was put into an oven and annealed again for 10 h at 550 °C for recrystallization.

2.2. Characterization Methods

The morphology of $\text{CuO@CuFe}_2\text{O}_4$ arrays was examined by SEM using a Carl Zeiss Sigma HV workstation (GmbH, Oberkochen, Germany). The microscope was equipped with a Gemini electron column with an energy-selective backscattered detector and energy-dispersive X-ray spectrometer with Bruker Quantax XFlash 6 | 10 detector (GmbH, Karlsruhe, Germany). UV-Vis spectroscopy was conducted using a Jasco V-650 spectrophotometer equipped with a 60 mm integrating sphere (Jasco, Easton, MD, USA). Size distribution was performed using ImageJ software (<https://imagej.nih.gov/ij/>, accessed on 30 December 2021). Powder X-ray diffraction was performed on samples on FTO glass and data were collected on an X'Pert PRO MPD powder diffractometer (manufactured by Panalytical B.V. Netherlands) using $\text{Co-K}\alpha$ (with Fe filter) radiation equipped with a fast detector. Then, 2θ was converted to that of $\text{Cu-K}\alpha$. The crystal structure was refined based on data obtained from the XRD pattern using the VESTA 3 software, National Museum of Nature and Science, 4-1-1, Amakubo, Tsukuba-shi, Ibaraki 305-0005, Japan [23]. XPS measurements were performed using a Microlab 350 (Thermo Electron, East Grinstead, UK) spectrometer, which was equipped with a dual Al/Mg anode. The X-ray radiation source ($\text{Al-K}\alpha$) at 1486.6 eV was used for investigations of the following parameters: power 300 W, voltage 15 kV, emission current 20 mA. All the XPS spectra for individual elements were recorded at a pass energy 40 eV, energy step size 0.1 eV. Advantage software (Version 5.9911, Thermo Fisher Scientific, Waltham, MA, USA) for data processing was used to perform the deconvolution procedure by using an asymmetric Gaussian/Lorentzian mixed function at a

constant G/L ratio equal 0.35 (± 0.05). The measured binding energies were corrected in reference to the energy of C 1s peak at 285.0 eV.

2.3. PEC Measurement

A conventional three-electrode system consisting of CuO@CuFe₂O₄ deposited on FTO glass as the working electrode, a platinum wire as the counter electrode, and an Ag/AgCl reference electrode in saturated KCl solution were implemented in 0.1 M NaOH electrolyte solution (pH 13). The electrolyte was purged with N₂ for 35 min before every measurement to remove O₂. Electrochemical potentials were converted to the RHE scale ($E_{(RHE)} = E_{(Ag/AgCl)} + E_{(Ag/AgCl)}^0 + 0.059 \times pH$ where $E_{(Ag/AgCl)}^0 = 0.175$ V and pH = 13). The working electrodes were polarized at 10 mV/s by a CHI660D potentiostat. Simulated AM 1.5 G (100 m·W·cm⁻²) illumination was obtained with an Oriel 150 W solar simulator (LoT Quantum Design, Darmstadt, Germany). The IPCE vs. excitation wavelength graphs were obtained using light from a 500 W Xenon lamp and a Multispec 257 monochromator (Oriel) with a typical bandwidth of 4 nm. The absolute light intensity passing through the monochromator was measured with an OL 730-5C UV-enhanced silicon detector (Gooch& Housego, Darmstadt, Germany). The current versus potential (J-E) plots of CuO@CuFe₂O₄ photocathodes were measured in a Teflon cell equipped with a quartz window. The exposed CuO@CuFe₂O₄ electrode surface area was 0.28 cm².

3. Results and Discussion

3.1. Characterization

The morphology of CuFe PBAs and CuFe₂O₄ after electrodeposition and heat treatment were characterized by scanning electron microscope (SEM), as shown in Figure 1. Before annealing, the sample consisted of cubic nanoparticles (NPs) typical of PBAs [19]. The layer of Cu[Fe(CN)₆] was observed to be dense and uniform thickness-wise due to the nature of the synthetic method, but not homogeneous. After annealing, the grains retained their density but changed in shape, from cubic NPs to amorphous shape with an average size of approximately 28.84 ± 4.03 nm (Figure S1), confirming the conversion of CuFe PBAs to CuFe₂O₄. The particles appeared to be more homogeneous size-wise than its starting materials due to the breakdown of larger Cu[Fe(CN)₆] NPs caused by the elimination of the C≡N bonds. The thickness of the films remained mostly the same after thermal conversion. The energy-dispersive spectroscopy (EDS) analysis showed the ratio of the components before thermal treatment (CuFe₂O₄ (Figure S2) are Cu: 0.4; Fe: 0.24; C :1.44; and N: 2.1, indicating the formation of the CuFe PBA and the excess of Cu was the unreacted residual. After annealing, the composition of the film was Cu: 0.41; Fe: 0.28; O: 1.2 confirming the composition of spinel oxides CuO@CuFe₂O₄ (Figure S3). The excessive amount of O in the structure was mostly due to the initial porosity of Cu[Fe(CN)₆].

EDS mapping shown in Figure 2 revealed that Fe was positioned on the outer shell of the NPs while Cu and O could be observed all over the whole particles. This indicated that, during electrosynthesis, the outer shell of the Cu grain reacted with [Fe^{III}(CN)₆] to form Cu[Fe(CN)₆] while the inner core remained Cu. In a typical PBA structure, defect sites are present where the vacancies of M-CN are completed by water molecules. Upon thermal treatment, these sites were most likely where the breaking down of the precursors Cu@Cu[Fe(CN)₆] happened during the formation of the core-shell structures. The outer shell formed CuFe₂O₄ and the core formed CuO.

The formation of CuO@CuFe₂O₄ could be confirmed by X-ray diffraction (XRD) pattern as presented in Figure 3. The major diffraction peaks can be indexed as (220), (103), (311), (312), (511), and (440) of the tetragonal CuFe₂O₄ (JCPDS No. 34-0425) and the peaks of CuO (JCPDS No. 80-1917) at (111/200) and (202). All the peaks were well defined, indicating the good crystallinity of the film. The peaks of Fe₂O₃ (JCPDS No. 33-0664) at (012), (104), and (113) were also observed on the XRD pattern.

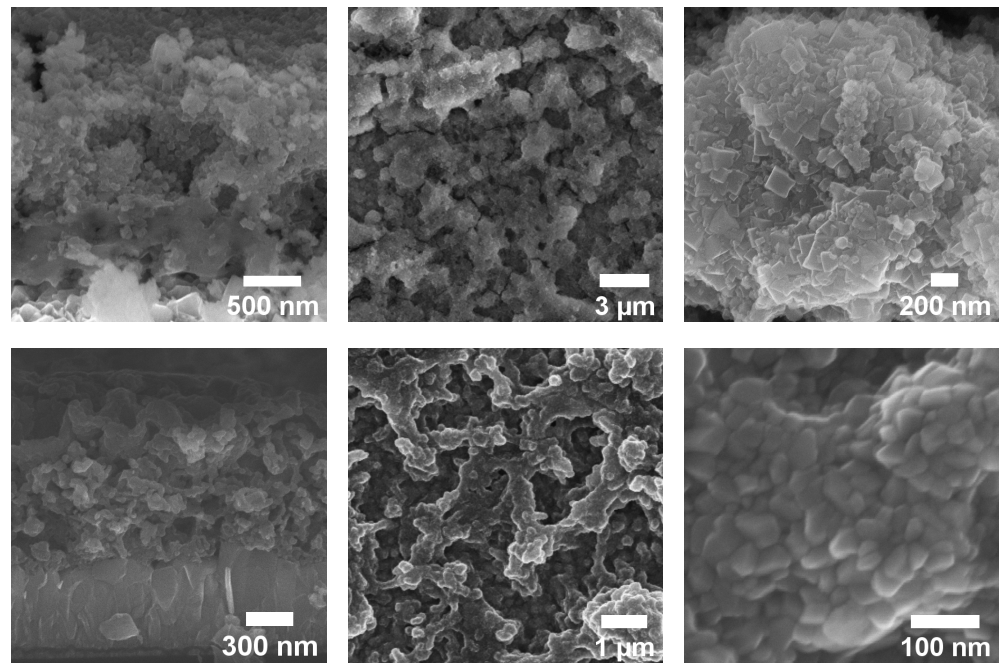


Figure 1. SEM imaging of Cu@CuFe PBAs (top images) and CuO@CuFe₂O₄ (bottom images).

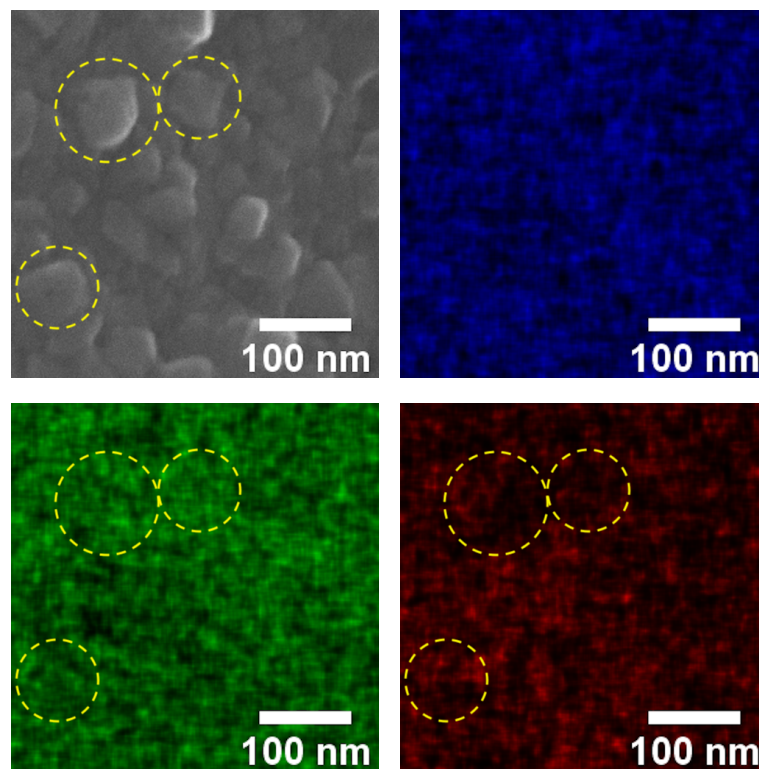


Figure 2. EDS mapping of Cu, Fe, and O on the CuO@CuFe₂O₄ layer. (mark circles indicated the mapping at the same positions).

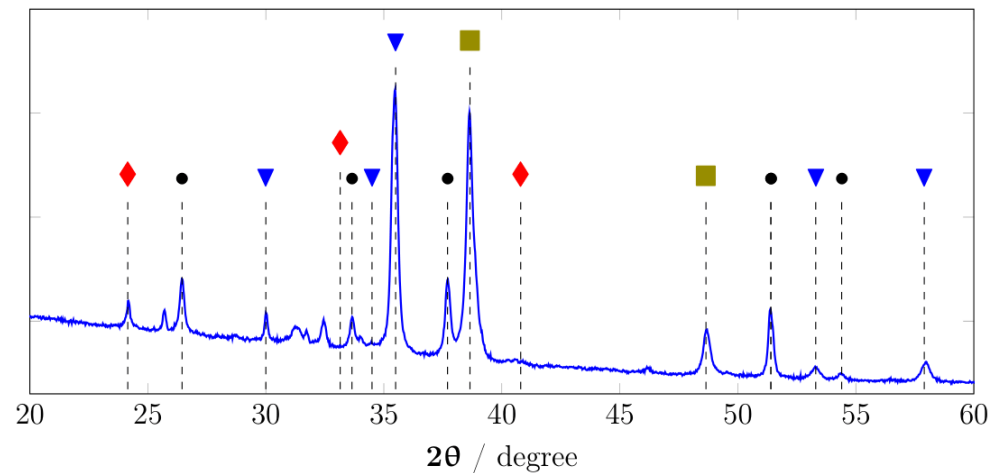


Figure 3. XRD patterns of CuO@CuFe₂O₄ (● = FTO, ▼ = CuFe₂O₄, ◆ = Fe₂O₃, and ■ = CuO).

Grain sizes obtained by Scherrer equation from the XRD pattern:

$$D = \frac{k \times \lambda}{\beta \times \cos \theta} \quad (1)$$

where $k = 0.94$, $\lambda = 1.54 \text{ \AA}$, and β is the full-width half-maximum in radian, calculated to be 28.09 nm for the CuFe₂O₄ domain which was in great agreement with the grain sizes observed on SEM indicating its single crystallinity. The CuO domain was calculated to be 26.6 nm, which was slightly smaller than that of CuFe₂O₄. This again confirmed the core-shell structure of CuO@CuFe₂O₄.

The lattice constant of the tetragonal CuFe₂O₄ shell were calculated using the following relation [24]:

$$\frac{1}{d^2} = \frac{(h^2 + k^2)}{a^2} + \frac{l^2}{c^2} \quad (2)$$

where a and c are lattice parameters, (hkl) is the miller indices, and d is the interplanar distance. The lattice parameter a value for the tetragonal CuFe₂O₄ shell was calculated to be 8.41 Å which is much greater than the reported values of ~5.9 Å for tetragonal CuFe₂O₄ [24,25]. In addition, the c parameter of CuFe₂O₄ was determined to be 8.0 Å, slightly smaller than that of previously reported values of 8.4 Å [24,25]. This was due to the fact that the CuFe₂O₄ shell conserved most of the structure of PBAs, which had a face-centered cubic with a unit parameter at approximately 10 Å, making them excellent precursors for nanoporous metal oxides. Upon thermal conversion, the C≡N bonds were eliminated and substituted by O, leading to the shortening of the bond length between two metal centers.

Figure 4 shows the high-resolution core-level XPS spectra of the CuO@CuFe₂O₄ sample. The shape of the Cu2p spectrum (left) suggested that the copper was in an oxidized state. Apart from the Cu2p_{3/2} and Cu2p_{1/2} peaks, the satellite lines characteristic of Cu²⁺ in CuO are clearly visible [26,27]. The deconvolution procedure used for the copper peak confirms the presence of CuO (Cu2p_{3/2}—932.7 eV and Cu2p_{1/2}—952.5 eV) as well as the CuFe₂O₄ compound (Cu2p_{3/2}—934.4 eV and Cu2p_{1/2}—954.6 eV) [28,29]. The spectral line at 934.4 eV can also be attributed to copper hydroxide or copper sulfate [28,29], but the presence of these compounds is unlikely. This is due to the fact that the produced material was annealed twice after being prepared at 400 and 550 °C. The high resolution Fe2p spectrum (right) clearly indicates the presence of Fe oxide bonds in the investigated material, which can be assigned to the Fe³⁺ (710.6 eV, 724.1 eV) [30,31] and Fe²⁺ (708.9 eV and 722.6) [30,31] peaks. This was also confirmed by the shape of the iron Fe2p spectral line, where characteristic satellite lines from the detected oxides are visible [32]. For the

recorded iron peak (Fe2p), the satellite lines are unusual. In particular, the lines that are located between the Fe2p_{3/2} and Fe2p_{1/2} peaks are too intense. This is due to the presence of a tin signal (Sn3p_{3/2}) [31] at this point which comes from the sample substrate (FTO). Further considering the spectrum of Fe2p, the peaks at 712.5 and 726.2 eV might suggest the presence of copper ferrite [28,29]. Therefore, the obtained XPS results are consistent with the XRD measurements, which confirm the core-shell structure of the material.

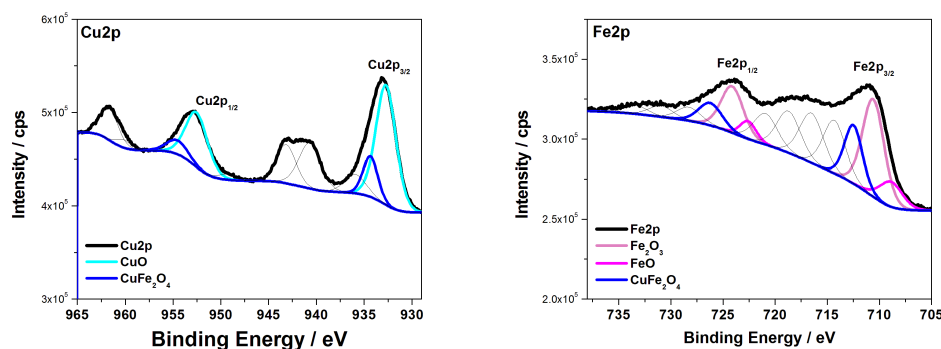


Figure 4. XPS high-resolution spectra of Cu2p (left) and Fe2p (right) for the CuO@CuFe₂O₄ sample after the deconvolution procedure.

3.2. Optical Properties

The UV-Vis spectra and Tauc plot of the direct bandgap of CuO@CuFe₂O₄ are presented in Figure 5. The bandgap energy of CuO@CuFe₂O₄ was found to be 1.5 eV larger than the value reported by Kezzim et al. [5] which was due to the presence of CuO in the core. The larger bandgap could also be due to the smaller crystal sizes of the NPs [33]. On the other hand, the UV-Vis spectra was shown to have an absorption band in the visible light range.

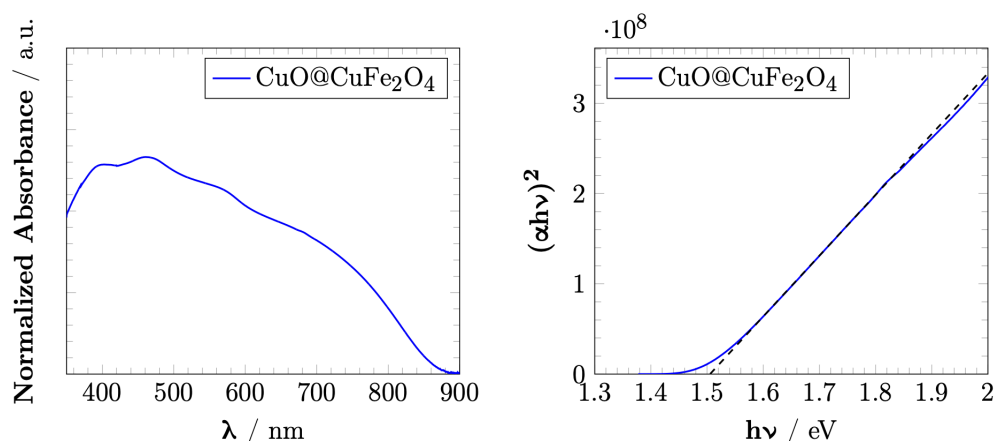


Figure 5. Normalized UV-Vis absorbance band of CuFe₂O₄ (left) and the Tauc plot of the direct optical band gap of CuFe₂O₄ (right).

3.3. Photoelectrochemical Properties

Figure 6A shows the linear sweeping voltammetry (LSV) of the CuO@CuFe₂O₄ electrode in N₂-saturated NaOH 0.1 M solution under chop light irradiation. The photoelectrode was shown to have a maximum photocurrent density of approximately -1 mA/cm^2 at 0.3 V vs. RHE with a clear cathodic characteristic of p-type materials. Chronoamperometry measurements Figure 6B (right) at 0.5 V vs. RHE showed that the electrode had a photocurrent density of approximately -0.35 mA/cm^2 with no corrosion observed, which is quite unusual for Cu-based materials [34]. Extended chronoamperometry measurements

during one hour (Figure S5) showed that the electrode retained approximately 30% of its current density with almost no photocorrosion.

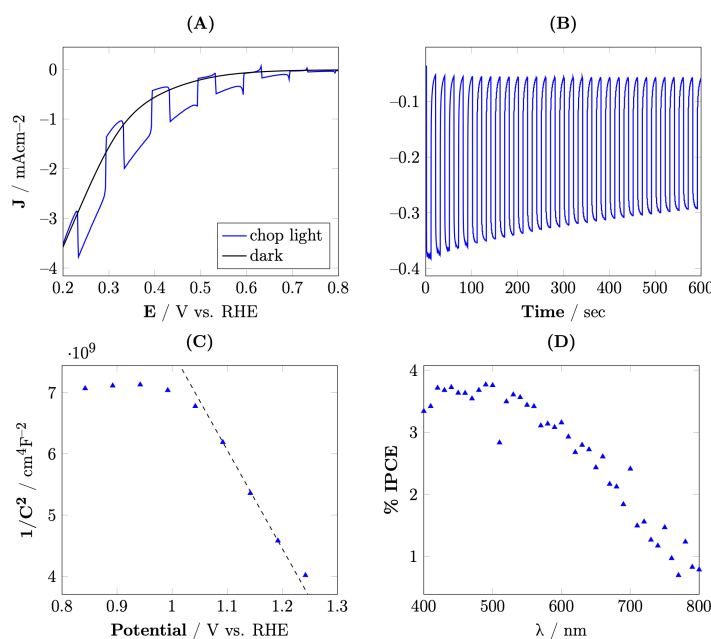


Figure 6. (A) Cathodic LSV scan of CuO@CuFe₂O₄ under chop light irradiation in 0.1 M NaOH (pH 13) with N₂ purged; (B) i-T curve of CuO@CuFe₂O₄ under chop light irradiation at 0.5 V vs. RHE in 0.1 M NaOH (pH 13); (C) Mott–Schottky plot of CuO@CuFe₂O₄ in 0.1 M NaOH (pH 13); (D) IPCE spectrum of CuO@CuFe₂O₄ measured at 0.5 V vs. RHE in 0.1 M NaOH (pH 13).

Mott–Schottky measurement of CuO@CuFe₂O₄ is presented in Figure 6C. The flatband potential (E_{fb}) of the materials was evaluated using Mott–Schottky analysis. A negative slope was observed for CuO@CuFe₂O₄ demonstrating p-type semiconductor behavior of the photoelectrode. For a p-type semiconductor, E_{fb} is generally located near the valence band [35] and it can be estimated from the intersection of the plot of $1/C^2$ vs. E by the following equation:

$$\frac{1}{C^2} = \frac{2}{e\epsilon\epsilon_0 N} \left(E - E_{fb} - \frac{kT}{e} \right) \quad (3)$$

where C is the capacitance, e is the electron charge, ϵ is the dielectric constant, ϵ_0 is permittivity of vacuum, N is acceptor density, E is the electrode potential, k is the Boltzmann constant, and T is the temperature. E_{fb} was estimated to be 1.27 V vs. RHE. Since the bandgap of CuO@CuFe₂O₄ was determined to be 1.5 eV, the band position was indeed in the range for H₂ production.

The impedance Nyquist plot in Figure S5 clearly shows only one semicircle characteristic that proves that the charge transfer process occurs between the solid phase and the electrolyte. Therefore, the water reduction process takes place on the CuFe₂O₄ surface. The charge transfer resistance between phases of CuO and CuFe₂O₄ is negligible, which proves that the obtained core–shell structure holds a very good adhesion. If the water photoreduction process took place over CuO phase, a second semicircle of characteristics would be visible in the diagram. Thus, CuFe₂O₄ is a material that allows the transport of the generated charge without any significant losses because of charge recombination and charge accumulation at the surface, which in turn decreases the extent of CuO photocorrosion itself.

Figure 6D shows the *IPCE* spectrum of CuO@CuFe₂O₄. The %*IPCE* values were calculated using the following equation:

$$IPCE(\%) = 1239.7 \times \frac{J}{\lambda \times P} \times 100\% \quad (4)$$

where *J* is the photocurrent density, *P* is the intensity of the monochromatic light recorded with a power meter equipped with a thermopile detector and a calibrated silicon photodiode, and λ is the wavelength of the incident light. The %*IPCE* values reached their maximum value at approximately 420 nm and 490 nm with the value of 3.8%. The results showed that the %*IPCE* spectrum followed the trend of the UV–Vis absorption results.

4. Conclusions

In this study, core–shell CuO@CuFe₂O₄ was prepared using the facile method by thermal conversion from Cu@Cu[Fe(CN)₆] precursors. After annealing, the photoelectrode exhibited p-type semiconductor characteristics. The CuO exhibits a p-semiconductor nature, which is strongly dependent on the delocalized hole states occurring in function of the concentration of the Cu vacancies [36]. The conductivity of such a system in general is poor due to relatively low electron concentration in the conduction band combined with slow carrier mobility. However, the charge transfer mechanism applied to CuFe₂O₄ was assigned to the typical small polaron hopping of SC conduction band “d” [37]. The photocurrent density under chop light irradiation at 0.5 V vs. RHE was -0.35 mA/cm^2 , which retained 50% of that after one hour, showing great stability. The electrode showed only a small photocorrosion indicating a decrease in the electrons–holes recombination usually observed for this type of materials. A closer look at the crystal structure (Figure S6) showed an increase in cell volume due to the porosity of starting materials. Upon the elimination of the C≡N bonds and the substitution of O, the bond lengths between Cu and Fe ions were slightly shorter due to the formation of Cu–O and Fe–O bonds.

Supplementary Materials: The following supporting information can be downloaded at: <https://www.mdpi.com/article/10.3390/ma15031029/s1>, Figure S1: Size distribution of CuFe₂O₄ obtained from SEM imaging; Figure S2: EDS analysis of CuFe PBAs; Figure S3: EDS analysis of CuO@CuFe₂O₄; Figure S4: Extended i–T curve of CuO@CuFe₂O₄ in NaOH 0.1 M (pH 13) under chop light irradiation; Figure S5: Nyquist measurement of CuO@CuFe₂O₄ in NaOH 0.1 M (pH 13) under 1 sun light irradiation; Figure S6: Crystal structure of CuFe PBAs before and after thermal conversion; Figure S7: Images of the front and back side of prepared CuOCuFe₂O₄ sample.

Author Contributions: Conceptualization, L.T. and R.S.; methodology, L.T. and R.S.; validation, R.S.; formal analysis, L.T., K.B., P.W. and M.P.; investigation, L.T., A.P. and N.N.; writing—original draft preparation, L.T.; writing—review and editing, L.T. and R.S.; visualization, L.T.; supervision, R.S.; project administration, R.S.; funding acquisition, R.S. All authors have read and agreed to the published version of the manuscript.

Funding: This research was funded by the Polish National Science Center SONATA grant No. 2017/26/E/ST5/01137 awarded to R.S.

Institutional Review Board Statement: Not applicable.

Informed Consent Statement: Not applicable.

Data Availability Statement: The data presented in this study are available upon request from the corresponding author.

Acknowledgments: The authors thank Dominik Kurzydowski for his contribution to the work.

Conflicts of Interest: The authors declare no conflict of interest.

Sample Availability: Samples of the compounds CuO@CuFe₂O₄ are available from the authors.

References

1. Walter, M.G.; Warren, E.L.; McKone, J.R.; Boettcher, S.W.; Mi, Q.; Santori, E.A.; Lewis, N.S. Solar water splitting cells. *Chem. Rev.* **2010**, *110*, 6446–6473. [\[CrossRef\]](#)
2. Sivula, K. Solar-to-chemical energy conversion with photoelectrochemical tandem cells. *Chimia* **2013**, *67*, 155–161. [\[CrossRef\]](#)
3. Li, J.; Wu, N. Semiconductor-based photocatalysts and photoelectrochemical cells for solar fuel generation: A review. *Catal. Sci. Technol.* **2015**, *5*, 1360–1384. [\[CrossRef\]](#)
4. Jang, Y.J.; Lee, J.S. Photoelectrochemical Water Splitting with p-Type Metal Oxide Semiconductor Photocathodes. *ChemSusChem* **2019**, *12*, 1835–1845. [\[CrossRef\]](#)
5. Kezzim, A.; Nasrallah, N.; Abdi, A.; Trari, M. Visible light induced hydrogen on the novel hetero-system CuFe₂O₄/TiO₂. *Energy Convers. Manag.* **2011**, *52*, 2800–2806. [\[CrossRef\]](#)
6. Liu, Y.; He, H.; Li, J.; Li, W.; Yang, Y.; Li, Y.; Chen, Q. Preparation and enhanced photoelectrochemical performance of a p-n heterojunction CuFe₂O₄/WO₃ nanocomposite film. *RSC Adv.* **2015**, *5*, 99378–99384. [\[CrossRef\]](#)
7. Hussain, S.; Hussain, S.; Waleed, A.; Tavakoli, M.M.; Wang, Z.; Yang, S.; Fan, Z.; Nadeem, M.A. Fabrication of CuFe₂O₄/α-Fe₂O₃ Composite Thin Films on FTO Coated Glass and 3-D Nanospine Structures for Efficient Photoelectrochemical Water Splitting. *ACS Appl. Mater. Interfaces* **2016**, *8*, 35315–35322. [\[CrossRef\]](#)
8. Tarek, M.; Rezaul Karim, K.M.; Sarkar, S.M.; Deb, A.; Ong, H.R.; Abdullah, H.; Cheng, C.K.; Rahman Khan, M.M. Hetero-structure CdS–CuFe₂O₄ as an efficient visible light active photocatalyst for photoelectrochemical reduction of CO₂ to methanol. *Int. J. Hydrogen Energy* **2019**, *44*, 26271–26284. [\[CrossRef\]](#)
9. Liu, Y.; Le Formal, F.; Boudoire, F.; Yao, L.; Sivula, K.; Guijarro, N. Insights into the interfacial carrier behaviour of copper ferrite (CuFe₂O₄) photoanodes for solar water oxidation. *J. Mater. Chem. A* **2019**, *7*, 1669–1677. [\[CrossRef\]](#)
10. Saadi, S.; Bouguelia, A.; Trari, M. Photoassisted hydrogen evolution over spinel CuM₂O₄ (M=Al, Cr, Mn, Fe and Co). *Renew. Energy* **2006**, *31*, 2245–2256. [\[CrossRef\]](#)
11. Helaili, N.; Bessekhoud, Y.; Bachari, K.; Trari, M. Synthesis and physical properties of the CuFe_{2-x}Mn_xO₄ (0 ≤ x ≤ 2) solid solution. *Mater. Chem. Phys.* **2014**, *148*, 734–743. [\[CrossRef\]](#)
12. Díez-García, M.I.; Lana-Villarreal, T.; Gómez, R. Study of Copper Ferrite as a Novel Photocathode for Water Reduction: Improving Its Photoactivity by Electrochemical Pretreatment. *ChemSusChem* **2016**, *9*, 1504–1512. [\[CrossRef\]](#)
13. Li, X.; Liu, A.; Chu, D.; Zhang, C.; Du, Y.; Huang, J.; Yang, P. High performance of manganese porphyrin sensitized p-type CuFe₂O₄ photocathode for solar water splitting to produce hydrogen in a tandem photoelectrochemical cell. *Catalysts* **2018**, *8*, 108. [\[CrossRef\]](#)
14. Zhang, E.; Wang, L.; Zhang, B.; Xie, Y.; Wang, G. Shape-controlled hydrothermal synthesis of CuFe₂O₄ nanocrystals for enhancing photocatalytic and photoelectrochemical performance. *Mater. Chem. Phys.* **2019**, *235*, 121633. [\[CrossRef\]](#)
15. Tsege, E.L.; Atabaev, T.S.; Hossain, M.A.; Lee, D.; Kim, H.K.; Hwang, Y.H. Cu-doped flower-like hematite nanostructures for efficient water splitting applications. *J. Phys. Chem. Solids* **2016**, *98*, 283–289. [\[CrossRef\]](#)
16. Kyesmen, P.I.; Nombona, N.; Diale, M. Heterojunction of nanostructured α-Fe₂O₃/CuO for enhancement of photoelectrochemical water splitting. *J. Alloys Compd.* **2021**, *863*, 158724. [\[CrossRef\]](#)
17. Park, S.; Baek, J.H.; Zhang, L.; Lee, J.M.; Stone, K.H.; Cho, I.S.; Guo, J.; Jung, H.S.; Zheng, X. Rapid Flame-Annealed CuFe₂O₄ as Efficient Photocathode for Photoelectrochemical Hydrogen Production. *ACS Sustain. Chem. Eng.* **2019**, *7*, 5867–5874. [\[CrossRef\]](#)
18. Maitra, S.; Pal, S.; Maitra, T.; Halder, S.; Roy, S. Solvothermal Etching-Assisted Phase and Morphology Tailoring in Highly Porous CuFe₂O₄ Nanoflake Photocathodes for Solar Water Splitting. *Energy Fuels* **2021**, *35*, 14087–14100. [\[CrossRef\]](#)
19. Catala, L.; Mallah, T. Nanoparticles of Prussian blue analogs and related coordination polymers: From information storage to biomedical applications. *Coord. Chem. Rev.* **2017**, *346*, 32–61. [\[CrossRef\]](#)
20. Zakaria, M.B.; Hu, M.; Imura, M.; Salunkhe, R.R.; Umezawa, N.; Hamoudi, H.; Belik, A.A.; Yamauchi, Y. Single-crystal-like nanoporous spinel oxides: A strategy for synthesis of nanoporous metal oxides utilizing metal-cyanide hybrid coordination polymers. *Chem. A Eur. J.* **2014**, *20*, 17375–17384. [\[CrossRef\]](#)
21. Xiao, L.; Youji, L.; Feitai, C.; Peng, X.; Ming, L. Facile synthesis of mesoporous titanium dioxide doped by Ag-coated graphene with enhanced visible-light photocatalytic performance for methylene blue degradation. *RSC Adv.* **2017**, *7*, 25314–25324. [\[CrossRef\]](#)
22. Lin, X.; Du, S.; Li, C.; Li, G.; Li, Y.; Chen, F.; Fang, P. Consciously Constructing the Robust NiS/g-C₃N₄ Hybrids for Enhanced Photocatalytic Hydrogen Evolution. *Catal. Letters* **2020**, *150*, 1898–1908. [\[CrossRef\]](#)
23. Momma, K.; Izumi, F. VESTA 3 for three-dimensional visualization of crystal, volumetric and morphology data. *J. Appl. Crystallogr.* **2011**, *44*, 1272–1276. [\[CrossRef\]](#)
24. Yadav, R.S.; Havlica, J.; Masilko, J.; Kalina, L.; Wasserbauer, J.; Hajdúchová, M.; Enev, V.; Kuřitka, I.; Kožáková, Z. Cation Migration-Induced Crystal Phase Transformation in Copper Ferrite Nanoparticles and Their Magnetic Property. *J. Supercond. Nov. Magn.* **2016**, *29*, 759–769. [\[CrossRef\]](#)
25. Chatterjee, B.K.; Bhattacharjee, K.; Dey, A.; Ghosh, C.K.; Chattopadhyay, K.K. Influence of spherical assembly of copper ferrite nanoparticles on magnetic properties: Orientation of magnetic easy axis. *Dalt. Trans.* **2014**, *43*, 7930–7944. [\[CrossRef\]](#)
26. Biesinger, M.C.; Payne, B.P.; Grosvenor, A.P.; Lau, L.W.; Gerson, A.R.; Smart, R.S.C. Resolving surface chemical states in XPS analysis of first row transition metals, oxides and hydroxides: Cr, Mn, Fe, Co and Ni. *Appl. Surf. Sci.* **2011**, *257*, 2717–2730. [\[CrossRef\]](#)

27. Biesinger, M.C. Advanced analysis of copper X-ray photoelectron spectra. *Surf. Interface Anal.* **2017**, *49*, 1325–1334. [[CrossRef](#)]
28. Liu, Y.; Zhang, H.; Fu, W.; Yang, Z.; Li, Z. Characterization of temperature sensitivity of V-modified CuFe₂O₄ ceramics for NTC thermistors. *J. Mater. Sci. Mater. Electron.* **2018**, *29*, 18797–18806. [[CrossRef](#)]
29. Zhang, E.; Wang, L.; Zhang, B.; Xie, Y.; Wang, G. Enhanced photocatalytic performance of polyvinylidene fluoride membrane by doped CuFe₂O₄ nanocrystals for water treatment. *J. Sol.-Gel. Sci. Technol.* **2020**, *93*, 452–461. [[CrossRef](#)]
30. Naumkin, A.; Kraut-Vass, A.; Gaarenstroom, S.W.; Powell, C. NIST X-ray Photoelectron Spectroscopy (XPS) Database, Version 4.1. <https://srdata.nist.gov/xps/> (accessed on 29 December 2021).
31. Moulder, J.F.; Stickle, W.F.; Sobol, P.E.; Bomben, K.D. *Handbook of X-ray Photoelectron Spectroscopy*; Perkin-Elmer: Boston, MA, USA, 1992; p. 262.
32. Grosvenor, A.P.; Kobe, B.A.; Biesinger, M.C.; McIntyre, N.S. Investigation of multiplet splitting of Fe2p XPS spectra and bonding in iron compounds. *Surf. Interface Anal.* **2004**, *36*, 1564–1574. [[CrossRef](#)]
33. Marotti, R.E.; Giorgi, P.; Machado, G.; Dalchiele, E.A. Crystallite size dependence of band gap energy for electrodeposited ZnO grown at different temperatures. *Sol. Energy Mater. Sol. Cells* **2006**, *90*, 2356–2361. [[CrossRef](#)]
34. Li, C.; He, J.; Xiao, Y.; Li, Y.; Delaunay, J.J. Earth-abundant Cu-based metal oxide photocathodes for photoelectrochemical water splitting. *Energy Environ. Sci.* **2020**, *10*, 3269–3306. [[CrossRef](#)]
35. Karim, K.M.R.; Ong, H.R.; Abdullah, H.; Yousuf, A.; Cheng, C.K.; Khan, M.M.R. Electrochemical study of copper ferrite as a catalyst for CO₂ photoelectrochemical reduction. *Bull. Chem. React. Eng. Catal.* **2018**, *13*, 236–244. [[CrossRef](#)]
36. Nolan, M.; Elliott, S.D. The p-type conduction mechanism in Cu₂O: A first principles study. *Phys. Chem. Chem. Phys.* **2006**, *8*, 5350–5358. [[CrossRef](#)] [[PubMed](#)]
37. Attia, S.; Helaili, N.; Bessekhoud, Y.; Trari, M. Visible Light Hydrogen Production on the Novel Ferrite CuFe₂O₄. In *Advances in Renewable Hydrogen and Other Sustainable Energy Carriers*; Springer: Singapore, 2021; pp. 105–112. [[CrossRef](#)]